

A Nonlinear Attitude Observer Based on Active Vision and Inertial Measurements

Sérgio Brás, *Student Member, IEEE*, Rita Cunha, José F. Vasconcelos, Carlos Silvestre, *Member, IEEE*, and Paulo Oliveira, *Member, IEEE*

Abstract—This paper presents an experimentally evaluated solution to the problem of estimating the attitude of a rigid body using rate gyros and a pan-tilt camera. A nonlinear attitude observer combines angular velocity measurements obtained from rate gyros with images of a planar scene provided by the camera. By directly exploiting the sensor information, a stabilizing feedback law is introduced, and exponential convergence to the origin of the estimation errors is shown. Additionally, an active-vision system is proposed that relies on an image-based exponentially input-to-state-stable control law for the pan and tilt angular rates of the camera to keep the features in the image plane. Using recent results in geometric numerical integration, a multirate implementation of the observer is proposed, which exploits the complementary bandwidth of the sensors. Practical considerations, such as the lens-distortion compensation and the computation of suitable observer feedback gains, are considered. Experimental results obtained with a high-accuracy motion rate table demonstrate the high level of performance attained by the proposed solution.

Index Terms—Estimation, navigation, nonlinear systems, observers, visual servoing.

I. INTRODUCTION

COMPUTER vision has long been recognized as an extremely flexible technique to sense the environment and to acquire valuable information for pose estimation and control. Over the past decades, awareness of this potential has brought about a widespread interest in the field of vision-based control and localization [1], [2]. The aim of this paper is the development of a nonlinear image-based observer to estimate the vehicle attitude relative to a set of image features.

The use of cameras as positioning sensors in robotics has its most significant representative in the body of work devoted to vision-based control (see, for example, [1]–[3] and references therein). The problem of pose estimation in computer vision has

also received a lot of attention. A variety of algebraic and iterative methods based on point or line correspondences have been proposed (see, for example, [4]). Although algorithms based solely on image measurements can determine the position and attitude of a camera, they can greatly benefit from the integration with inertial sensors, namely, rate gyros and accelerometers, as well as from the use of dynamic filtering and observer techniques [5]–[8]. In this paper, we follow a similar reasoning to obtain a nonlinear observer that combines rate gyros measurements with image measurements and estimates the attitude of a rigid body.

In many applications, it is appropriate to design observers based only on the rigid body kinematics, which are an exact description of the physical quantities involved. In this framework, the attitude of the vehicle is propagated by integrating inertial sensor measurements [9]–[11]. Research on the problem of deriving a stabilizing law for systems evolving on manifolds, where attitude is represented in its natural space as an element of the special orthogonal group $SO(3)$, can be found in [12]–[14]. These references provide important guidelines for observer design and discuss the topological limitations to achieving global stabilization on the $SO(3)$ manifold.

Nonlinear observers are usually formulated in the continuous-time domain, and the computational implementation of these algorithms calls for advanced discrete-time integration algorithms. The selection of a suitable numerical method is vital since it should preserve the geometric properties of the differential equations. Particular emphasis has been placed by the scientific community on methods for integration of differential equations evolving on Lie groups. These methods were originally proposed by Crouch and Grossman [15], and its general order conditions can be found in [16]. Munthe-Kaas in [17] constructed generalized Runge–Kutta methods for integration of differential equations evolving on Lie groups, where the computations are performed in the Lie algebra, which is a linear space. More recently, commutator-free Lie group methods were derived to overcome some of the problems associated with the computation of commutators [18], [19]. A comprehensive overview of geometric numerical integration methods and their application to multibody dynamics evolving on the special Euclidean group $SE(3)$ can be found in [20]. For more applications of Lie group methods, see [21].

In this study, we consider the problem of estimating the attitude of a rigid body equipped with a triad of rate gyros and a pan-and-tilt camera. The proposed attitude nonlinear observer fuses the angular velocity measurements from the angular velocity with the information given by images of a planar scene

Manuscript received October 19, 2010; revised December 16, 2010; accepted February 1, 2011. Date of publication March 28, 2011; date of current version August 10, 2011. This paper was recommended for publication by Associate Editor Il H. Suh and Editor W. K. Chung upon evaluation of the reviewers' comments. This work was supported in part by the Fundação para a Ciência e a Tecnologia (Institute for Systems and Robotics/Instituto Superior Técnico plurianual funding) through the PIDDAC Program funds, by Project PTDC/MAR/64546/2006 OBSERVFLY, and by the EU project TRIDENT of the EC-FP7. The work of S. Brás was supported by the Ph.D. Grant SFRH/BD/47456/2008 from Fundação para a Ciência e a Tecnologia

The authors are with the Institute for Systems and Robotics, Instituto Superior Técnico, 1049-001 Lisbon, Portugal (e-mail: sbras@isr.ist.utl.pt; rita@isr.ist.utl.pt; jvasconcelos@isr.ist.utl.pt; cjs@isr.ist.utl.pt; pjcro@isr.ist.utl.pt).

Color versions of one or more of the figures in this paper are available online at <http://ieeexplore.ieee.org>.

Digital Object Identifier 10.1109/TRO.2011.2112950

provided by an active vision system. By directly exploiting sensor information, a stabilizing feedback law is derived that guarantees exponential convergence to the origin of the estimation errors in the presence of constant bias disturbances on the rate gyro measurements. Moreover, for time-varying bias terms, the estimation errors are guaranteed to remain bounded, provided that the time derivative of the bias and the error on the initial estimates are sufficiently small.

The discrete-time implementation of the observer is specifically addressed. Using recent results from numerical analysis [15], a geometric integration method is adopted to approximate conveniently the original continuous-time observer. To exploit the high-frequency readings of the rate gyros, a multirate implementation of the observer is proposed, which updates the attitude estimate, while the image measurements are not available, and recomputes the estimate as soon as the time-delayed image measurements are available. As a second goal, we develop an active vision system that keeps the features inside the image plane using an image-based control law for the camera pan and tilt angular rates. Experimental results were obtained using a real prototype. The test trajectories were generated using a Model 2103HT from Ideal Aeromsmith [22], which is a three-axis motion rate table, which was specially designed to provide precise angular position, rate, and acceleration for the development and test of inertial components and systems.

Preliminary versions of the results described in this paper have appeared in [23] and [24]. This extended version contains new experimental results and proofs of theorems and lemmas, which are omitted in earlier versions.

The paper is structured as follows. In Section II, the attitude estimation and the camera pan-and-tilt control problems are introduced. The sensor suite is described and the reference frames adopted in the work are detailed. The attitude observer is presented in Section III, and its properties are highlighted. In Section IV, a camera pan-and-tilt input-to-state-stable (ISS) controller is derived, which centers the visual features in the image plane. A low-complexity discrete-time implementation of the observer is presented in Section V. A prototype working in real time is described in Section VI. In Section VII, simulations illustrate the performance of the observer and the pan-and-tilt controller, and experimental results are presented in Section VIII. Finally, concluding remarks are given in Section IX.

II. PROBLEM FORMULATION

Consider a rigid body equipped with a triad of rate gyros and a pan-and-tilt camera. Let $\{B\}$ be the reference frame attached to the rigid body, $\{L\}$ be the local reference frame attached to the feature plane, and $\{C\}$ be the camera reference frame with origin at the camera's center of projection with the z -axis aligned with the optical axis. The observed scene consists of four points whose coordinates in $\{L\}$ are denoted by ${}^L\mathbf{x}_i \in \mathbb{R}^3$, $i \in \{1, \dots, 4\}$. Without loss of generality, the origin of $\{L\}$ is assumed to coincide with the centroid of the feature points so that $\sum_{i=1}^4 {}^L\mathbf{x}_i = 0$. The special orthogonal group is given by the set $\text{SO}(n) := \{\mathbf{R} \in \mathbb{R}^{n \times n} : \mathbf{R}^T \mathbf{R} = \mathbf{I}, \det(\mathbf{R}) = 1\}$. The

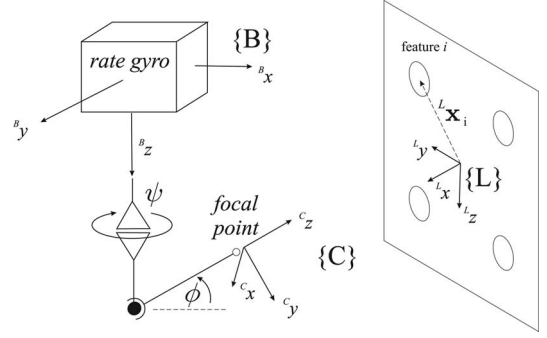


Fig. 1. Experimental setup.

image-based estimation problem, as illustrated in Fig. 1, can be summarized as the problem of estimating the attitude of a rigid body given by the rotation matrix from $\{B\}$ to $\{L\}$, which is denoted as ${}^L_B \mathbf{R} \in \text{SO}(3)$, using visual features and angular velocity readings. An image-based controller for the camera pan-and-tilt angular rates is also considered to keep the features in the image plane.

A. Sensor Suite

The triad of rate gyros is assumed to be aligned with $\{B\}$ so that it provides measurements of the body angular velocity $\boldsymbol{\omega}_B$ corrupted by a constant unknown bias term \mathbf{b}_ω :

$$\boldsymbol{\omega}_r = \boldsymbol{\omega}_B + \mathbf{b}_\omega, \quad \dot{\mathbf{b}}_\omega = 0.$$

As shown in Fig. 1, the camera can describe pan and tilt motions corresponding to the angles ψ and ϕ , respectively. As such the rotation matrix from $\{C\}$ to $\{B\}$ is given by

$$\begin{aligned} {}^B_C \mathbf{R} &= \mathbf{R}_{\text{pan}} \mathbf{R}_{\text{tilt}} \\ \mathbf{R}_{\text{pan}} &= \mathbf{R}_z(\pi/2 + \psi), \quad \mathbf{R}_{\text{tilt}} = \mathbf{R}_x(\pi/2 + \phi) \end{aligned} \quad (1)$$

where $\mathbf{R}_z(\cdot)$ and $\mathbf{R}_x(\cdot)$ denote rotation matrices about the z -axis and x -axis, respectively.

For simplicity of notation, let $\mathcal{R} = {}^L_C \mathbf{R}$ be the rotation matrix from $\{C\}$ to $\{L\}$ and \mathbf{p} be the position of the origin of $\{L\}$ with respect to $\{C\}$. Then, the 3-D coordinates of the feature points expressed in $\{C\}$ can be written as $\mathbf{q}_i = \mathcal{R}^T {}^L \mathbf{x}_i + \mathbf{p}$, $i \in \{1, \dots, 4\}$ and, using the perspective camera model [5], the 2-D image coordinates of those points $\mathbf{y}_i \in \mathbb{R}^2$ can be written as

$$\begin{bmatrix} \mathbf{y}_i \\ 1 \end{bmatrix} = \delta_i \mathbf{A} \mathbf{q}_i \quad (2)$$

where $\mathbf{A} \in \mathbb{R}^{3 \times 3}$ is the camera calibration matrix assumed to be known, and δ_i is an unknown scalar encoding depth information and given by

$$\delta_i = (\mathbf{e}_3^T \mathbf{q}_i)^{-1}, \quad \mathbf{e}_3 = [0 \ 0 \ 1]^T. \quad (3)$$

B. Attitude Kinematics

The camera frame attitude kinematics can be described by

$$\dot{\mathcal{R}} = \mathcal{R}[\boldsymbol{\omega}]_\times \quad (4)$$

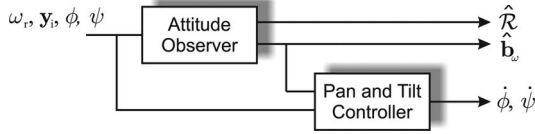


Fig. 2. Block diagram of the attitude observer and camera controller.

where for simplicity of notation, $\boldsymbol{\omega} \in \mathbb{R}^3$ denotes the camera angular velocity, and $[\mathbf{x}]_{\times}$ is the skew-symmetric matrix defined by the vector $\mathbf{x} \in \mathbb{R}^3$ such that $[\mathbf{x}]_{\times}\mathbf{y} = \mathbf{x} \times \mathbf{y}$, $\mathbf{y} \in \mathbb{R}^3$. Taking the time derivative of (1), straightforward computations show that $\boldsymbol{\omega}$ can be written as

$$\boldsymbol{\omega} = {}^C_B \mathbf{R} \boldsymbol{\omega}_B + \mathbf{R}_{\text{tilt}}^T [\dot{\phi} \ 0 \ \dot{\psi}]^T \quad (5)$$

where $\dot{\psi}$ and $\dot{\phi}$ are the time derivatives of the camera pan and tilt angles, respectively. Assuming that the camera pan and tilt angles are known, we can readily obtain the attitude of the rigid body from ${}^L_B \mathbf{R} = \mathcal{R}_B^C \mathbf{R}$.

C. Problem Summary

The estimation problem addressed in this paper can be stated as follows.

Problem 1: Consider the attitude kinematic model described by (4), and let $\hat{\mathcal{R}}$ and $\hat{\mathbf{b}}_{\omega}$ denote the estimates of \mathcal{R} and \mathbf{b}_{ω} , respectively. Design a dynamic observer for \mathcal{R} based on $\boldsymbol{\omega}_r$ and \mathbf{y}_i , $i = \{1, \dots, 4\}$, such that $\hat{\mathcal{R}}$ and $\hat{\mathbf{b}}_{\omega}$ converge to \mathcal{R} and \mathbf{b}_{ω} with the largest possible basin of attraction.

To develop an active vision system using the camera pan-and-tilt degrees of freedom, we consider the following problem.

Problem 2: Let $\bar{\mathbf{y}}$ be the image of the features' centroid given by

$$\begin{bmatrix} \bar{\mathbf{y}} \\ 1 \end{bmatrix} = \bar{\delta} \mathbf{A} \mathbf{p}, \quad \bar{\delta} = (\mathbf{e}_3^T \mathbf{p})^{-1}. \quad (6)$$

Design a control law for $\dot{\psi}$ and $\dot{\phi}$ based on $\boldsymbol{\omega}_r$ and \mathbf{y}_i , $i = \{1, \dots, 4\}$, such that $\bar{\mathbf{y}}$ approaches the center of the image plane.

Fig. 2 depicts the cascaded composition of the system, where the angular rate bias estimate is fed into the pan-and-tilt controller.

III. ATTITUDE OBSERVER

In this section, we propose a solution to Problem 1 that builds on results presented in [9], where a nonlinear position and attitude observer based on landmark measurements and biased velocity measurements was shown to provide exponential convergence to the origin for the position, velocity, attitude, and bias errors. The proposed observer is designed to match the rigid body attitude kinematics by taking the form

$$\dot{\hat{\mathcal{R}}} = \hat{\mathcal{R}}[\hat{\boldsymbol{\omega}}]_{\times} \quad (7)$$

where $\hat{\boldsymbol{\omega}}$ is the feedback term designed to compensate for the estimation errors. The attitude and bias estimation errors are defined as $\tilde{\mathcal{R}} = \hat{\mathcal{R}}\mathcal{R}^T$ and $\tilde{\mathbf{b}}_{\omega} = \hat{\mathbf{b}}_{\omega} - \mathbf{b}_{\omega}$, respectively. Using

(5) and (7), the rotation error dynamics can be written as

$$\dot{\tilde{\mathcal{R}}} = \tilde{\mathcal{R}}[\mathcal{R}(\hat{\boldsymbol{\omega}} - \boldsymbol{\omega})]_{\times}. \quad (8)$$

Some rotational degrees of freedom are unobservable in the case where features are all collinear, as discussed in [9] and references therein. The following necessary condition for attitude estimation based on image measurements is assumed.

Assumption 1: There are at least four features of which no three are collinear.

We will consider a feedback law for $\hat{\boldsymbol{\omega}}$ that uses measurements of the form

$$\mathbf{U} = \mathcal{R}^T [{}^L \mathbf{u}_1 \ \dots \ {}^L \mathbf{u}_5] \in \mathbb{R}^{3 \times 5} \quad (9)$$

where ${}^L \mathbf{u}_i \in \mathbb{R}^3$ are time-invariant in the local frame $\{L\}$. To obtain these vector readings from the image coordinates \mathbf{y}_i , we explore the geometry of planar scenes. For that purpose, we introduce the matrices

$$\mathbf{X} = [{}^L \mathbf{x}_1 \ \dots \ {}^L \mathbf{x}_4], \quad \mathbf{Y} = \begin{bmatrix} \mathbf{y}_1 & \dots & \mathbf{y}_4 \\ 1 & \dots & 1 \end{bmatrix}$$

where ${}^L \mathbf{x}_i$ are the 3-D coordinates of the feature points expressed in $\{L\}$, and \mathbf{y}_i the corresponding 2-D image coordinates. We can now state the following lemma.

Lemma 1: Let $\boldsymbol{\sigma} = [\sigma_1 \ \sigma_2 \ \sigma_3 \ \sigma_4]^T \in \mathbb{R}^4 \setminus \{0\}$ and $\boldsymbol{\rho} = [\rho_1 \ \rho_2 \ \rho_3 \ \rho_4]^T \in \mathbb{R}^4 \setminus \{0\}$ be such that $\mathbf{Y}\boldsymbol{\sigma} = \mathbf{0}$, $\mathbf{X}\boldsymbol{\rho} = \mathbf{0}$, and $\mathbf{1}^T \boldsymbol{\rho} = 0$, where $\mathbf{1} = [1 \ 1 \ 1 \ 1]^T$. Suppose that the features verify Assumption 1 and that the camera configuration is such that the image is not degenerate (neither a point nor a line). Then, the depth variables δ_i defined in (3) can be written as

$$\delta_i = \alpha \frac{\rho_i}{\sigma_i}$$

where $\alpha \in \mathbb{R}$, $\rho_i \neq 0$, and $\sigma_i \neq 0$ for $i \in \{1, 2, 3, 4\}$.

Proof: From (2), \mathbf{Y} and \mathbf{X} are related by the expression $\mathbf{Y} = \mathbf{A}(\mathcal{R}^T \mathbf{X} + \mathbf{p}\mathbf{1}^T)\mathbf{D}_{\delta}$, where $\mathbf{D}_{\delta} = \text{diag}(\boldsymbol{\delta})$, $\boldsymbol{\delta} = [\delta_1 \ \delta_2 \ \delta_3 \ \delta_4]^T$ and $\mathbf{1} = [1 \ 1 \ 1 \ 1]^T$. The notation $\text{diag}(\mathbf{a})$ describes a diagonal matrix formed by placing the elements of $\mathbf{a} \in \mathbb{R}^n$ in the main diagonal. Let \mathbf{n} be a unit vector perpendicular to the features plane, such that $\mathbf{n}^T \mathbf{n} = 1$ and $\mathbf{X}^T \mathbf{n} = \mathbf{0}$; then

$$\begin{aligned} \mathbf{Y} &= \mathbf{A}(\mathcal{R}^T \mathbf{X} + \mathbf{p}\mathbf{1}^T)\mathbf{D}_{\delta} \\ &= \mathbf{A}(\mathcal{R}^T (\mathbf{n}\mathbf{n}^T - [\mathbf{n}]_{\times}^2)\mathbf{X} + \mathbf{p}\mathbf{n}^T \mathbf{n}\mathbf{1}^T)\mathbf{D}_{\delta} \\ &= \mathbf{A}\mathbf{M}(\mathbf{X} + \mathbf{n}\mathbf{1}^T)\mathbf{D}_{\delta} \end{aligned} \quad (10)$$

where $\mathbf{M} = (-\mathcal{R}^T([\mathbf{n}]_{\times})^2 + \mathbf{p}\mathbf{n}^T)$ is nonsingular for camera configurations that do not lead to degenerate images (i.e., straight lines and points). Using (10), we can write

$$\mathbf{Y}\boldsymbol{\sigma} = \mathbf{0} \Leftrightarrow (\mathbf{X} + \mathbf{n}\mathbf{1}^T)\mathbf{D}_{\delta}\boldsymbol{\sigma} = \mathbf{0} \quad (11)$$

and since $\mathbf{X}\boldsymbol{\rho} = \mathbf{0}$, and $\mathbf{1}^T \boldsymbol{\rho} = 0$, we have $(\mathbf{X} + \mathbf{n}\mathbf{1}^T)\boldsymbol{\rho} = \mathbf{0}$. In addition, if no three points are collinear, we have the following.

- 1) The null spaces of $\mathbf{X} + \mathbf{n}\mathbf{1}^T$ and \mathbf{Y} have dimension one.
- 2) For any vector $\boldsymbol{\rho} = [\rho_1 \ \rho_2 \ \rho_3 \ \rho_4]^T \neq \mathbf{0}$ such that $\mathbf{X}\boldsymbol{\rho} = \mathbf{0}$ and $\mathbf{1}^T \boldsymbol{\rho} = 0$, the inequality $\prod_{j=1}^4 \rho_j \neq 0$ also holds.
- 3) For any vector $\boldsymbol{\sigma} = [\sigma_1 \ \sigma_2 \ \sigma_3 \ \sigma_4]^T \neq \mathbf{0}$ such that $\mathbf{Y}\boldsymbol{\sigma} = \mathbf{0}$, the inequality $\prod_{j=1}^4 \sigma_j \neq 0$ also holds.

Then, from (11) and $(\mathbf{X} + \mathbf{n}\mathbf{1}^T)\boldsymbol{\rho} = 0$, we can conclude that $\mathbf{D}_\delta\boldsymbol{\sigma} = \alpha\boldsymbol{\rho} \Leftrightarrow \boldsymbol{\delta} = \alpha\mathbf{D}_\sigma^{-1}\boldsymbol{\rho}$, where $\alpha \in \mathbb{R}$ and $\mathbf{D}_\sigma = \text{diag}(\boldsymbol{\sigma})$.

Writing (2) in matrix form and using Lemma 1, we obtain

$$\mathbf{Y} = \mathbf{A}(\mathcal{R}^T\mathbf{X} - \mathbf{p}\mathbf{1}^T)\alpha\mathbf{D}_\sigma^{-1}\mathbf{D}_\rho$$

where $\mathbf{D}_\rho = \text{diag}(\boldsymbol{\rho})$. From the constraint on the centroid of the features $\mathbf{X}\mathbf{1} = 0$, it follows that

$$\alpha\mathcal{R}^T\mathbf{X} = \mathbf{A}^{-1}\mathbf{Y}\mathbf{D}_\rho^{-1}\mathbf{D}_\sigma \left(\mathbf{I} - \frac{1}{4}\mathbf{1}\mathbf{1}^T \right)$$

which takes the form of (9) up to a scale factor. We can use the properties of the rotation matrix and the positive depth constraint $\delta_i > 0$ to obtain the normalized vector readings

$${}^C\bar{\mathbf{x}}_i = \mathcal{R}^T L \bar{\mathbf{x}}_i = \text{sign}(\alpha) \frac{\alpha \mathcal{R}^T L \mathbf{x}_i}{\|\alpha \mathcal{R}^T L \mathbf{x}_i\|} \quad (12)$$

where $\text{sign}(\alpha) = \text{sign}(\rho_i/\sigma_i)$, and ${}^L\bar{\mathbf{x}}_i = {}^L\mathbf{x}_i/\|{}^L\mathbf{x}_i\|$, $i = \{1, \dots, 4\}$, and $\|\mathbf{a}\|$, $\mathbf{a} \in \mathbb{R}^n$, denotes the Euclidean norm of vectors. Finally, we define the matrix \mathbf{U} using linear combinations of (12) so that $\mathbf{U} = {}^C\bar{\mathbf{X}}\mathbf{A}_X$, where $\mathbf{A}_X \in \mathbb{R}^{5 \times 5}$ is nonsingular, and ${}^C\bar{\mathbf{X}} = [{}^C\bar{\mathbf{x}}_1, \dots, {}^C\bar{\mathbf{x}}_4, {}^C\bar{\mathbf{x}}_i \times {}^C\bar{\mathbf{x}}_j]$ for any linearly independent ${}^C\bar{\mathbf{x}}_i$ and ${}^C\bar{\mathbf{x}}_j$.

The directionality associated with the features positions is made uniform by defining transformation \mathbf{A}_X such that $\mathbf{U}\mathbf{U}^T = \mathbf{I}$. The desired \mathbf{A}_X exists if Assumption 1 is satisfied [9].

A. Observer Design

Let the bias in angular velocity measurements be constant, i.e., $\dot{\mathbf{b}}_\omega = \mathbf{0}$, and consider the Lyapunov function

$$V = \frac{\|\tilde{\mathcal{R}} - \mathbf{I}\|^2}{2} + \frac{1}{2k_{b_\omega}} \|\tilde{\mathbf{b}}_\omega\|^2 \quad (13)$$

where $k_{b_\omega} > 0$ and $\|\cdot\|$ denote the Frobenius norm for matrices and the Euclidean norm for vectors. Since $\tilde{\mathcal{R}}$ is a rotation matrix, V can also be written as

$$V = \text{tr}(\mathbf{I} - \tilde{\mathcal{R}}) + \frac{1}{2k_{b_\omega}} \|\tilde{\mathbf{b}}_\omega\|^2.$$

To compute the time derivative of V , it is convenient to define the unskew operator $[\cdot]_\otimes$, which verifies $[[\mathbf{a}]_\times]_\otimes = \mathbf{a}$, $\mathbf{a} \in \mathbb{R}^3$. Using (8) and noting that $\text{tr}(\mathbf{A}[\mathbf{b}]_\times) = -[\mathbf{A} - \mathbf{A}^T]_\otimes^T \mathbf{b}$, we obtain

$$\dot{V} = \mathbf{s}_\omega^T (\hat{\omega} - \boldsymbol{\omega}) + \frac{1}{k_{b_\omega}} \dot{\tilde{\mathbf{b}}}_\omega^T \tilde{\mathbf{b}}_\omega \quad (14)$$

where $\mathbf{s}_\omega = \mathcal{R}^T [\tilde{\mathcal{R}} - \tilde{\mathcal{R}}^T]_\otimes$. The feedback term \mathbf{s}_ω can be expressed as an explicit function of the sensor readings

$$\begin{aligned} \mathbf{s}_\omega &= \mathcal{R}^T [\tilde{\mathcal{R}} - \tilde{\mathcal{R}}^T]_\otimes \\ &= [(\hat{\mathcal{R}}^T L \bar{\mathbf{X}} \mathbf{A}_X) \mathbf{U}^T - \mathbf{U} (\hat{\mathcal{R}}^T L \bar{\mathbf{X}} \mathbf{A}_X)^T]_\otimes \\ &= \left[\sum_{i=1}^5 \hat{\mathcal{R}}^T L \bar{\mathbf{X}} \mathbf{A}_X \mathbf{e}_i (\mathbf{U} \mathbf{e}_i)^T - (\mathbf{U} \mathbf{e}_i) (\hat{\mathcal{R}}^T L \bar{\mathbf{X}} \mathbf{A}_X \mathbf{e}_i)^T \right]_\otimes \\ &= \sum_{i=1}^5 (\hat{\mathcal{R}}^T L \bar{\mathbf{X}} \mathbf{A}_X \mathbf{e}_i) \times (\mathbf{U} \mathbf{e}_i) \end{aligned}$$

where ${}^L\bar{\mathbf{X}} = [{}^L\bar{\mathbf{x}}_1, \dots, {}^L\bar{\mathbf{x}}_4, {}^L\bar{\mathbf{x}}_i \times {}^L\bar{\mathbf{x}}_j]$, for i and j that verify ${}^L\bar{\mathbf{X}} = \mathcal{R}^C \bar{\mathbf{X}}$, and where \mathbf{e}_i is the unit vector such that $e_i = 1$. Let $\hat{\omega}$ define the following attitude feedback law:

$$\begin{aligned} \hat{\omega} &= {}^C_B \mathbf{R} (\boldsymbol{\omega}_r - \hat{\mathbf{b}}_\omega + \mathbf{R}_{\text{pan}}^T [\dot{\phi} \ 0 \ \dot{\psi}]^T) - k_\omega \mathbf{s}_\omega \\ &= {}^C_B \mathbf{R} (\boldsymbol{\omega}_B - \tilde{\mathbf{b}}_\omega + \mathbf{R}_{\text{pan}}^T [\dot{\phi} \ 0 \ \dot{\psi}]^T) - k_\omega \mathbf{s}_\omega \end{aligned} \quad (15)$$

where $k_\omega > 0$. Applying (15) in (14) and defining

$$\dot{\tilde{\mathbf{b}}}_\omega := k_{b_\omega} {}^B_C \mathbf{R} \mathbf{s}_\omega \quad (16)$$

the derivative of the Lyapunov function derivative becomes $\dot{V} = -k_\omega \|\mathbf{s}_\omega\|^2$. Considering the feedback law (15) and the update law (16), the closed-loop attitude error dynamics can be written as

$$\begin{aligned} \dot{\tilde{\mathcal{R}}} &= -k_\omega \tilde{\mathcal{R}} (\tilde{\mathcal{R}} - \tilde{\mathcal{R}}^T) - \tilde{\mathcal{R}} [\mathcal{R}_B^C \mathbf{R} \tilde{\mathbf{b}}_\omega]_\times \\ \dot{\tilde{\mathbf{b}}}_\omega &= k_{b_\omega} {}^B_C \mathbf{R} \mathcal{R}^T [\tilde{\mathcal{R}} - \tilde{\mathcal{R}}^T]_\otimes. \end{aligned} \quad (17)$$

The following lemma provides sufficient conditions for the boundedness of the estimation errors and excludes convergence to the equilibrium points satisfying $\|\tilde{\mathcal{R}} - \mathbf{I}\|^2 = 8$. Global asymptotic stability of the origin is precluded by topological limitations associated with those points [25].

Lemma 2: For any initial condition that satisfies

$$\frac{\|\tilde{\mathbf{b}}_\omega(t_0)\|^2}{8 - \|\tilde{\mathcal{R}}(t_0) - \mathbf{I}\|^2} < k_{b_\omega} \quad (18)$$

the estimation error $\tilde{\mathbf{x}} = (\tilde{\mathcal{R}}, \tilde{\mathbf{b}}_\omega)$ is bounded, and $\|\tilde{\mathcal{R}}(t) - \mathbf{I}\|^2 < 8$ for all $t \geq t_0$.

Proof: Let $\Omega_\rho = \{\tilde{\mathbf{x}} \in D : V \leq \rho\}$. As the Lyapunov function (18) is a weighted distance from the origin, $\exists \gamma \|\tilde{\mathbf{x}}\|^2 \leq \gamma V$, and Ω_ρ is a compact set. $\dot{V} \leq 0$ implies that any trajectory that starts in Ω_ρ remains in Ω_ρ . Therefore, $\forall t \geq t_0 \|\tilde{\mathbf{x}}(t)\|^2 \leq \gamma V(\tilde{\mathbf{x}}(t_0))$, and the state is bounded.

The gain condition (18) is equivalent to $V(\tilde{\mathbf{x}}(t_0)) < 4$. The invariance of Ω_ρ implies that $V(\tilde{\mathbf{x}}(t)) \leq V(\tilde{\mathbf{x}}(t_0))$. Therefore, $(1/2)\|\tilde{\mathcal{R}}(t) - \mathbf{I}\|^2 \leq V(\tilde{\mathbf{x}}(t_0)) < 4$, and consequently, $\|\tilde{\mathcal{R}}(t) - \mathbf{I}\|^2 < 8$ for all $t > t_0$.

Exploiting the results derived for linear time-varying (LTV) systems in [26], we can show that the trajectories of the system (17) converge to the desired equilibrium point.

Theorem 1: If $\boldsymbol{\omega}$ is bounded and $\tilde{\mathbf{b}}_\omega = 0$, then the attitude and bias estimation errors converge exponentially fast to the equilibrium point $(\tilde{\mathcal{R}}, \tilde{\mathbf{b}}_\omega) = (\mathbf{I}, 0)$ for any initial condition satisfying (18).

Proof: Let the attitude error be given in the quaternion form $\tilde{\mathbf{q}} = [\tilde{\mathbf{q}}_q^T \tilde{q}_s]^T$, where $\tilde{\mathbf{q}}_q = \frac{[\tilde{\mathcal{R}} - \tilde{\mathcal{R}}^T]_\otimes}{2\sqrt{1 + \text{tr}(\tilde{\mathcal{R}})}}$, and $q_s = \frac{1}{2}\sqrt{1 + \text{tr}(\tilde{\mathcal{R}})}$. The closed-loop dynamics are given by

$$\begin{aligned} \dot{\tilde{\mathbf{q}}}_q &= \frac{1}{2} \mathbf{Q}(\tilde{\mathbf{q}}) (-\mathcal{R}_B^C \mathbf{R} \tilde{\mathbf{b}}_\omega - 4k_\omega \tilde{\mathbf{q}}_q \tilde{q}_s) \\ \dot{\tilde{\mathbf{b}}}_\omega &= 4k_{b_\omega} {}^B_C \mathbf{R} \mathcal{R}^T \mathbf{Q}^T(\tilde{\mathbf{q}}) \tilde{\mathbf{q}}_q \end{aligned} \quad (19)$$

where $\mathbf{Q}(\tilde{\mathbf{q}}) := \tilde{q}_s \mathbf{I} + [\tilde{\mathbf{q}}_q]_\times$, and $\dot{\tilde{q}}_s = -2k_\omega \tilde{\mathbf{q}}_q^T \tilde{\mathbf{q}}_q \tilde{q}_s - \frac{1}{2} \tilde{\mathbf{q}}_q^T \mathcal{R}_B^C \mathbf{R} \tilde{\mathbf{b}}_\omega$. Using $\|\tilde{\mathbf{q}}_q\|^2 = \frac{1}{8} \|\tilde{\mathcal{R}} - \mathbf{I}\|^2$, the Lyapunov

function in quaternion form is given by $V = 4\|\tilde{\mathbf{q}}_q\|^2 + (1/2k_{b_\omega})\|\tilde{\mathbf{b}}_\omega\|^2$.

Given the coordinate transformation proposed in [11], let $\mathbf{x}_q := (\tilde{\mathbf{q}}_q, \tilde{\mathbf{b}}_\omega)$, $\mathbf{x}_q \in D_q$, and $D_q := \mathbf{B}(3) \times \mathbb{R}^3$, where $\mathbf{B}(3)$ is the 3-dimensional ball such that $\mathbf{B}(3) := \{\mathbf{x} \in \mathbb{R}^3 : \mathbf{x}^T \mathbf{x} \leq 1\}$, and define the system (19) in domain $D_q = \{\mathbf{x}_q \in D_q : V < 4\}$. The set D_q corresponds to the interior of a Lyapunov surface; therefore, it is well defined and positively invariant. Condition (18) implies that the initial state is contained in D_q .

Let $\mathbf{x}_* := (\tilde{\mathbf{q}}_{q*}, \tilde{\mathbf{b}}_{\omega*})$ and $D_q := \mathbb{R}^3 \times \mathbb{R}^3$, and define the linear time-varying system

$$\dot{\mathbf{x}}_* = \begin{bmatrix} \mathcal{A}(t, \lambda) & \mathcal{B}^T(t, \lambda) \\ -\mathcal{C}(t, \lambda) & \mathbf{0}_{3 \times 3} \end{bmatrix} \mathbf{x}_* \quad (20)$$

where $\lambda \in \mathbb{R}_0^+ \times D_q$, and the submatrices are described by $\mathcal{A}(t, \lambda) = -2k_\omega \tilde{q}_s(t, \lambda) \mathbf{Q}(\tilde{\mathbf{q}}(t, \lambda))$, $\mathcal{B}(t, \lambda) = -\frac{1}{2} \mathbf{B} \mathbf{R} \mathcal{R}^T \mathbf{Q}^T(\tilde{\mathbf{q}}(t, \lambda))$, $\mathcal{C}(t, \lambda) = -4 \mathbf{C} \mathbf{R} \mathcal{R}^T \mathbf{Q}^T(\tilde{\mathbf{q}}(t, \lambda))$, and $\tilde{\mathbf{q}}(t, \lambda)$ represents the solution of (19) with initial condition $\lambda = (t_0, \tilde{\mathbf{q}}(t_0), \tilde{\mathbf{b}}_\omega(t_0))$. The matrices $\mathcal{A}(t, \lambda)$, $\mathcal{B}(t, \lambda)$, and $\mathcal{C}(t, \lambda)$ are bounded, and the system is well defined.

If the parameterized system is λ -uniformly globally exponentially stable (λ -UGES), then (19) is uniformly exponentially stable in D_q [26, pp. 14–15]. The parameterized system verifies the assumptions of [26] as follows.

- 1) For bounded ω , the elements of $\mathcal{B}(t, \lambda)$, and $\frac{\partial \mathcal{B}(t, \lambda)}{\partial t}$ are bounded.
- 2) The positive-definite matrices $P(t, \lambda) = 8k_{b_\omega} \mathbf{I}$ and $Q(t, \lambda) = 32k_{b_\omega} \tilde{q}_s^2(t, \lambda) k_\omega \mathbf{I}$ satisfy $P(t, \lambda) \mathcal{B}^T(t, \lambda) = \mathcal{C}^T(t, \lambda)$, $-Q(t, \lambda) = \mathcal{A}^T(t, \lambda) P(t, \lambda) + P(t, \lambda) \mathcal{A}(t, \lambda) + \dot{P}(t, \lambda)$ and are bounded, namely, $q_m \mathbf{I} \leq Q(t, \lambda) \leq q_M \mathbf{I}$, where $q_M = 32k_\omega k_{b_\omega}$, and $q_m = q_M \min_{\mathbf{x}_q \in D_q} (1 - \|\tilde{\mathbf{q}}_q\|^2)$.

The system (20) is λ -UGES if and only if $\mathcal{B}(t, \lambda)$ is λ -uniformly persistently exciting [26]. In order to guarantee this, the sufficient condition $\mathcal{B}(\tau, \lambda) \mathcal{B}^T(\tau, \lambda) \geq \alpha_B \mathbf{I}$ is shown, for $\alpha_B > 0$, to be independent of τ and λ . Given that

$$\begin{aligned} 4\mathbf{y} \mathcal{B}(\tau, \lambda) \mathcal{B}^T(\tau, \lambda) \mathbf{y}^T &= \|\mathbf{y}\|^2 - (\mathbf{y}^T \mathbf{B} \mathbf{R} \mathcal{R} \tilde{\mathbf{q}}_q)^2 \\ &\geq \|\mathbf{y}\|^2 (1 - \|\tilde{\mathbf{q}}_q\|^2) \geq \|\mathbf{y}\|^2 \min_{\mathbf{x}_q \in D_q} (1 - \|\tilde{\mathbf{q}}_q\|^2) \end{aligned}$$

then $\mathcal{B}(\tau, \lambda) \mathcal{B}^T(\tau, \lambda)$ is lower bounded, and the persistency of the excitation condition is satisfied. Consequently, the parameterized system (20) is λ -UGES, and the nonlinear system (19) is exponentially stable in the domain D_q .

Remark 1: Note that the conditions of Lemma 2 and Theorem 1 are not restrictive, since ω is intrinsically bounded due to the practical limitation on the energy of the system, and (18) can always be satisfied inside the almost global domain of attraction by tuning the gains.

If the constant bias assumption is lifted, the convergence result of Theorem 1 no longer holds. However, it can be shown that for $\|\tilde{\mathbf{b}}_\omega\| < \gamma$, the estimation errors are bounded with ultimate bound proportional to γ .

Lemma 3: Consider the attitude observer defined in (17), and assume that ω and $\tilde{\mathbf{b}}_\omega$ are bounded, with $\|\tilde{\mathbf{b}}_\omega\| < \gamma$. Then, for a sufficiently small γ , there is a sufficiently small error on the

initial estimates such that the estimation errors are bounded with ultimate bound proportional to γ .

Proof: Let $\mathbf{x}_q = (2\tilde{\mathbf{q}}_v, (1/\sqrt{2k_{b_\omega}})\tilde{\mathbf{b}}_\omega)$, $V(\mathbf{x}_q) = 4\|\tilde{\mathbf{q}}_v\|^2 + (1/2k_{b_\omega})\|\tilde{\mathbf{b}}_\omega\|^2$, and $\mathbf{x}_{q0} = \mathbf{x}_q(t_0)$, and define the domain $U = \{\mathbf{x}_q : V(\mathbf{x}_q) \leq 4 - \epsilon\}$, $0 < \epsilon < 4$. From Theorem 1, we know that if k_b satisfies (18) and $\tilde{\mathbf{b}}_\omega = \mathbf{0}$, \mathbf{x}_q converges exponentially fast to zero inside the domain U . Then, by the converse Lyapunov theorem for systems with an exponentially stable equilibrium point [27], there is a Lyapunov function V_q such that $c_1 \|\mathbf{x}_q\|^2 \leq V_q(t, \mathbf{x}_q) \leq c_2 \|\mathbf{x}_q\|^2$, $\dot{V}_q(t, \mathbf{x}_q) \leq -c_3 \|\mathbf{x}_q\|^2$, and $\|(\partial V_q / \partial \mathbf{x}_q)\| \leq c_4 \|\mathbf{x}_q\|$, for $\mathbf{x}_q \in U$. It follows that if $\tilde{\mathbf{b}}_\omega \neq \mathbf{0}$, the time derivative of V_q satisfies

$$\dot{V}_q \leq -c_3 \|\mathbf{x}_q\|^2 + c_4 \kappa \|\mathbf{x}_q\| \|\tilde{\mathbf{b}}_\omega\| \quad (21)$$

where $\kappa = 1/\sqrt{2k_{b_\omega}}$. Assuming that $\|\tilde{\mathbf{b}}_\omega\| < \gamma$, (21) implies that $\dot{V}_q < 0$ for $\|\mathbf{x}_q\| > (c_4/c_3)\kappa\gamma$ and $\|\mathbf{x}_q\| < \sqrt{4 - \epsilon}$. If γ is sufficiently small, then we can guarantee that $(c_4/c_3)\kappa\gamma < \sqrt{(c_1/c_2)(4 - \epsilon)} < \sqrt{4 - \epsilon}$. Then, for every initial condition $\|\mathbf{x}_q(t_0)\| < \sqrt{(c_1/c_2)(4 - \epsilon)}$, $\mathbf{x}_q(t)$ remains in U for all $t \geq t_0$. Since $\dot{V}_q < 0$ for $(c_4/c_3)\kappa\gamma < \|\mathbf{x}_q\| < \sqrt{4 - \epsilon}$, we can conclude that \mathbf{x}_q is ultimately bounded by $\sqrt{(c_2/c_1)(c_4/c_3)\kappa\gamma}$.

Remark 2: Although Lemma 3 does not provide an expression for the bound on the bias derivative, it shows that this bound exists and that the estimation errors will remain bounded for time-varying rate gyro bias. In Section VII, we present simulation results that corroborate this behavior and indicate that the bounds on $\|\tilde{\mathbf{b}}_\omega\|$ and on the initial conditions are adequate for practical purposes. In addition, note that Lemma 3 can be adapted to account for band-limited noise, since the time derivative of the bias terms can also be interpreted as the time derivative of additive noise on the rate gyros measurements.

IV. CAMERA PAN-AND-TILT CONTROLLER

In this section, we address the problem of keeping the features inside the image plane, thereby exploiting the camera's ability to describe pan-and-tilt angular motions. As stated in Problem 2, the strategy adopted to achieve this goal amounts to controlling the camera pan and tilt angular velocities $\dot{\psi}$ and $\dot{\phi}$ using the image measurements \mathbf{y}_i and the angular velocity readings ω_r directly to keep the image of the features' centroid at a close distance from the center of the image plane.

We resort to Lyapunov theory and consider the following candidate Lyapunov function:

$$W = \frac{1}{2} \mathbf{p}^T \Pi \mathbf{p} = \frac{1}{2} (p_x^2 + p_y^2) \quad (22)$$

where $\mathbf{p} = [p_x \ p_y \ p_z]^T$ is the position of $\{L\}$ expressed in $\{C\}$, and $\Pi \in \mathbb{R}^{3 \times 3}$ is the x - y plane projection matrix. Using the expression for ω given in (5), the camera position kinematics can be written as

$$\begin{aligned} \dot{\mathbf{p}} &= [\mathbf{p}]_\times \omega - \mathbf{v} \\ &= [\mathbf{p}]_\times (\mathbf{R}_{\text{tilt}}^T \mathbf{R}_{\text{pan}}^T \omega_B + \mathbf{R}_{\text{tilt}}^T [\dot{\phi} \ 0 \ \dot{\psi}]^T) - \mathbf{v} \end{aligned} \quad (23)$$

where \mathbf{v} is the camera linear velocity. Recall that by definition, \mathbf{p} coincides with the position of the features' centroid and that

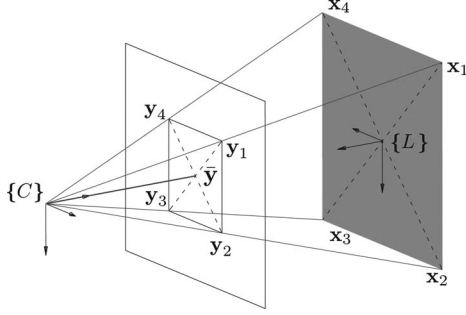


Fig. 3. Projection of the visual features in the image plane.

according to (6), its image is given by $\bar{\mathbf{y}}$. Therefore, by guaranteeing that the Lyapunov function W is decreasing, or equivalently, $[p_x \ p_y]$ is approaching the origin, we can ensure that $\bar{\mathbf{y}}$ is approaching the center of the image plane. To simplify the notation and without loss of generality, it is assumed from now onward that $\mathbf{A} = \mathbf{I}$ so that $\bar{y}_x = p_x/p_z$ and that $\bar{y}_y = p_y/p_z$.

Before proceeding to define the pan-and-tilt control laws, we highlight the fact that $\bar{\mathbf{y}}$ can be easily obtained from the image measurements \mathbf{y}_i . By noting that the feature centroid lies at the intersection between the vectors $\mathbf{x}_3 - \mathbf{x}_1$ and $\mathbf{x}_4 - \mathbf{x}_2$, and the intersection between lines is clearly an image invariant, we can immediately conclude that $\bar{\mathbf{y}}$ coincides with the point at the intersection between $\mathbf{y}_3 - \mathbf{y}_1$ and $\mathbf{y}_4 - \mathbf{y}_2$ (see Fig. 3).

Lemma 4: Let the camera position kinematics be described by (23), and assume that the rigid body and camera motions are such that $p_z > 0$ and $\cos \phi \neq 0$. Let the control law for the camera pan and tilt angular velocities be given by

$$\begin{bmatrix} \dot{\phi} \\ \dot{\psi} \end{bmatrix} = k_c \begin{bmatrix} 0 & -1 \\ \frac{1}{\cos \phi} & 0 \end{bmatrix} \bar{\mathbf{y}} - \begin{bmatrix} 1 & 0 & 0 \\ 0 & \tan \phi & 1 \end{bmatrix} \mathbf{R}_{\text{pan}}^T \hat{\boldsymbol{\omega}}_B \quad (24)$$

where $\hat{\boldsymbol{\omega}}_B = \boldsymbol{\omega}_r - \hat{\mathbf{b}}_\omega$, and $k_c > 0$. Then, the time derivative of the Lyapunov function W along the system trajectories satisfies

$$\dot{W} \leq -(k_c - \epsilon)W \quad \forall \|\Pi\mathbf{p}\| \geq \frac{1}{\epsilon}(\|\Pi\mathbf{v}\| + p_z \|\tilde{\mathbf{b}}_\omega\|) \quad (25)$$

and $0 < \epsilon < k_c$.

Proof: Taking the time derivative of (22) and using the expressions for $\dot{\mathbf{p}}$ given in (23), we obtain

$$\begin{aligned} \dot{W} &= \mathbf{p}^T \Pi([\mathbf{e}_3]_\times p_z \boldsymbol{\omega} - \mathbf{v}) \\ &= p_z [p_y \ -p_x \ 0] \mathbf{R}_{\text{tilt}}^T (\mathbf{R}_{\text{pan}}^T \boldsymbol{\omega}_B + [\dot{\phi} \ 0 \ \dot{\psi}]^T) - \mathbf{p}^T \Pi \mathbf{v}. \end{aligned}$$

Choosing $\dot{\phi}$ and $\dot{\psi}$ such that

$$\mathbf{R}_{\text{tilt}}^T (\mathbf{R}_{\text{pan}}^T \hat{\boldsymbol{\omega}}_B + [\dot{\phi} \ 0 \ \dot{\psi}]^T) = -k_c [-\bar{y}_y \ \bar{y}_x \ \kappa]^T \quad (26)$$

for some κ and noting that $\boldsymbol{\omega}_B = \hat{\boldsymbol{\omega}}_B - \tilde{\mathbf{b}}_\omega$, \dot{W} takes the form

$$\dot{W} = -k_c W - \mathbf{p}^T \Pi(\mathbf{v} + p_z [\mathbf{e}_3]_\times \tilde{\mathbf{b}}_\omega)$$

and consequently, (25) holds. Solving (26) for $\dot{\phi}$, $\dot{\psi}$, and κ , we obtain the control law (24).

Remark 3: If we apply the control law (24) to the system with state $\Pi\mathbf{p} = [p_x \ p_y]^T$ and interpret \mathbf{v} and $p_z \tilde{\mathbf{b}}_\omega$ as inputs, it

follows from (25) that the system is exponentially ISS. As such, the distance between the image of the centroid $\bar{\mathbf{y}}$ and the origin is ultimately bounded by $\|\Pi\mathbf{v}/p_z\|$ and $\|\tilde{\mathbf{b}}_\omega\|$ and converges exponentially fast to that bound. Moreover, if $\Pi\mathbf{v}/p_z$ and $\tilde{\mathbf{b}}_\omega$ converge to zero, so does $\bar{\mathbf{y}}$.

The proposed camera pan-and-tilt controller presents some noteworthy differences with respect to classical visual-servoing schemes, such as the image-based visual servo (IBVS) solution that uses the image coordinates of four coplanar points [1].

Comparing the control law (24) and an IBVS scheme with actuation on the pan and tilt angular rates, both approaches guarantee exponential decay of the error, provided that \mathbf{v} and $\tilde{\mathbf{b}}_\omega$ converge to zero. However, the traditional IBVS solution uses the inverse of the error Jacobian matrix, which introduces singularities and problems with local minima [1], which are not present in (24). Moreover, (24) relies solely on the image coordinates $\bar{\mathbf{y}}$, whereas using the inverse of the Jacobian matrix would require reconstruction of the depth coordinate p_z .

V. IMPLEMENTATION

In this section, we describe the computational implementation of the attitude observer proposed in Section III and camera's pan-and-tilt controller derived in Section IV.

A. Discrete-Time Algorithm

Cameras typically have much lower sampling rates than inertial sensors. To accommodate the different sampling rates, we adopt a multirate strategy. The complementary bandwidth characteristics of the camera and the rate gyros can be explored to obtain attitude estimates that are high bandwidth due to the inertial sensors and converge to zero due to the correction term provided by the vision system. This implementation can be seen as a prediction–correction algorithm. As illustrated in the flowchart shown in Fig. 4, while an image is being processed and the attitude feedback cannot be applied, the attitude estimate $\hat{\mathcal{R}}$ is propagated using solely the angular velocity readings $\boldsymbol{\omega}_r$. As soon as the image data are available, $\hat{\mathcal{R}}$ is recomputed using both $\boldsymbol{\omega}_r$ and the vector readings ${}^C\bar{\mathbf{X}}$. Note that, with this approach, the lag associated with the acquisition and processing of the visual information does not degrade the estimates accuracy. Moreover, this algorithm increases the intersampling accuracy of the estimates, which may be of critical importance for control purposes.

Several techniques can be adopted for discretization of differential equations. The choice of the algorithm depends on the specific problem, and stability and convergence are seldom guaranteed. The integration method should guarantee that the discrete-time implementation conveniently approximates the original continuous-time observer. Classic Runge–Kutta methods cannot be correctly applied to rotation matrix dynamics since polynomial invariants like the determinant of degree three or greater are not preserved in general [28, Th. IV-3.3]. An alternative is to apply a method that intrinsically preserves orthogonality like a Lie group integrator.

The attitude observer comprises the differential equations (7) and (16), with $\hat{\boldsymbol{\omega}}$ given by (15), and evolve on $\text{SO}(3)$ and

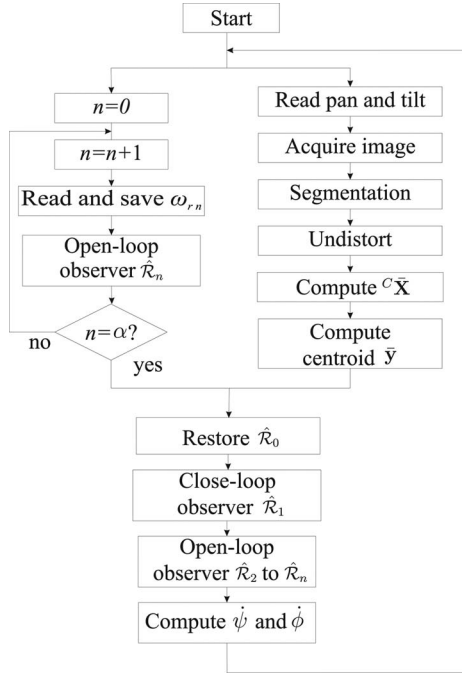


Fig. 4. Algorithm flowchart.

\mathbb{R}^3 , respectively. The first is integrated resorting to a geometric numerical integration method, namely, the Crouch–Grossman method (CG) [15], the Munthe-Kaas method (MK) [17], or the commutator-free Lie group method (CF) [18]. The second is implemented in discrete-time using a classic numerical integration technique.

The geometric numerical integration algorithm may require the knowledge of the function $\hat{\omega}(\cdot)$ at instants between sampling times. Alternative sampling and computation strategies can be adopted to obtain an approximation of this function, such as polynomial interpolation of the sampled data. Such techniques can significantly increase the computational cost undermining implementations in real time. Moreover, the unit is equipped with low-cost sensors that do not justify the use of high-order methods, and the computational resources are limited. Hence, we chose to implement a second-order geometric numerical method because it eliminates the need for intersampling interpolation, and therefore, it reduces the computational burden.

Let the sampling period of the rate gyros be $T \in \mathbb{R}^+$, and suppose, for convenience, that the sampling period of the camera measurements is αT , where α is an integer greater or equal to one. The discrete-time implementation of the bias estimator (16) is obtained by using a second-order *Adams–Bashford method*, which is a multistep method and, hence, suitable for sampled data. For further details, see [29]. The resulting numerical integration algorithm can be summarized as

$$\hat{\mathbf{b}}_{\omega \alpha k} = \hat{\mathbf{b}}_{\omega \alpha(k-1)} + \alpha T k_{b_{\omega}} (3/2^B \mathbf{R}_{\alpha(k-1)} \mathbf{s}_{\omega \alpha(k-1)} - 1/2^B \mathbf{R}_{\alpha(k-2)} \mathbf{s}_{\omega \alpha(k-2)}).$$

TABLE I
NUMBER OF ELEMENTARY OPERATIONS IN EACH STEP FOR SECOND-ORDER CG AND MK METHODS

operation	+	×	/	√	trig
CG 2 nd order	732	948	4	2	2
MK 2 nd order	732	946	5	3	3

This part of the algorithm is performed at the lower sampling frequency of $1/\alpha T$, since \mathbf{s}_{ω} is function of the camera measurements.

To choose between the CF, CG, and MK methods to numerically integrate (7), we took into account the computational cost of each method. The CF technique was discarded because it does not contemplate second-order implementations and higher order algorithms are very computation intensive. As for the second-order CG and MK methods, their coefficients can be obtained from [20] and [28]. These numerical integration techniques make use of the following operations: exponential map $\text{Exp}(\cdot)$ and inverse of the differential of the exponential map $\text{Dexp}^{-1}(\cdot)$, which, on $\text{SO}(3)$, can be implemented using the explicit forms given by

$$\text{Exp}(\mathbf{w}) = \mathbf{I} + \frac{\sin(\|\mathbf{w}\|)}{\|\mathbf{w}\|} [\mathbf{w}]_{\times} + \frac{\sin^2(\|\mathbf{w}\|/2)}{\|\mathbf{w}\|^2/2} ([\mathbf{w}]_{\times})^2$$

$$\text{Dexp}^{-1}(\mathbf{w}) = \mathbf{I} - \frac{1}{2} [\mathbf{w}]_{\times} - \frac{\|\mathbf{w}\| \cot(\|\mathbf{w}\|/2) - 2}{2\|\mathbf{w}\|^2} ([\mathbf{w}]_{\times})^2$$

where $\mathbf{w} \in \mathbb{R}^3$, and $\mathbf{w} \neq \mathbf{0}$. If $\mathbf{w} = \mathbf{0}$, $\text{Exp} = \text{Dexp}^{-1} = \mathbf{I}$. The number of elementary operations required to implement each step of these methods is summarized in Table I for the following operations: addition (+), multiplication (×), division (/), square root (√), and trigonometric function (trig). From this table, we can conclude that both methods have similar computational costs. Implementing the attitude observer resorting to the CG method, we obtain

$$\begin{aligned} \mathbf{s}_{\omega}^{(1)} &= \sum_{i=1}^5 (\hat{\mathcal{R}}_{k-1}^T L \bar{\mathbf{X}} \mathbf{A}_X \mathbf{e}_i) \times (\mathbf{U}_{k-1} \mathbf{e}_i) \\ \hat{\omega}^{(1)} &= \frac{C}{B} \mathbf{R}_{k-1}^T (\omega_{r \ k-1} - \hat{\mathbf{b}}_{\omega \ k-1} + \mathbf{R}_{\text{pan},k-1} [\dot{\phi} \ 0 \ \dot{\psi}]^T) \\ &\quad - \alpha k_{\omega} \mathbf{s}_{\omega}^{(1)} \\ Y &= \hat{\mathcal{R}}_{k-1} \text{Exp}(T \hat{\omega}^{(1)}) \\ \mathbf{s}_{\omega}^{(2)} &= \sum_{i=1}^5 (Y^T L \bar{\mathbf{X}} \mathbf{A}_X \mathbf{e}_i) \times (\mathbf{U}_k \mathbf{e}_i) \\ \hat{\omega}^{(2)} &= \frac{C}{B} \mathbf{R}_k^T (\omega_{r \ k} - \hat{\mathbf{b}}_{\omega \ k} + \mathbf{R}_{\text{pan},k} [\dot{\phi} \ 0 \ \dot{\psi}]^T) - \alpha k_{\omega} \mathbf{s}_{\omega}^{(2)} \\ \hat{\mathcal{R}}_k &= \hat{\mathcal{R}}_{k-1} \text{Exp}\left(\frac{T}{2} \hat{\omega}^{(1)}\right) \text{Exp}\left(\frac{T}{2} \hat{\omega}^{(2)}\right) \end{aligned}$$

where the feedback terms $\mathbf{s}_{\omega}^{(1)}$ and $\mathbf{s}_{\omega}^{(2)}$ are set to zero when the camera measurements are not available.

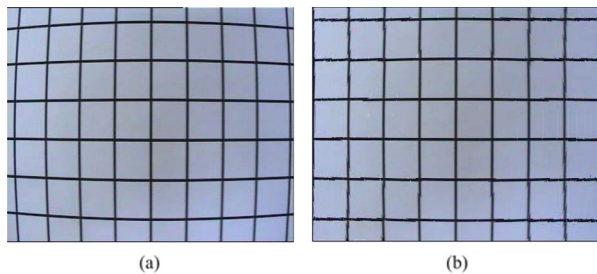


Fig. 5. Experimental results for compensation of the image distortion. (a) Original image. (b) Image with distortion compensation.

B. Lens Distortion

Camera lens often introduce distortion in the captured images. The most common distortion effects are the so-called barrel distortion and pincushion distortion [30]. Real lenses usually display a combination of these two effects.

When distortion is present, the mapping function between the 3-D world coordinates and the image coordinates provided by the perspective-camera model is no longer valid. Usually, the radial distortion is the main source of errors, and therefore, a nonlinear inverse radial function is applied. This function maps the image coordinates to those that would have been obtained with the ideal lens.

Let the distorted-image coordinates and the undistorted-image coordinates be denoted as (y_x^d, y_y^d) and (y'_x, y'_y) , respectively. These coordinates are referred to a reference frame with origin in the image distortion center. The inverse radial-distortion function can be written as a Taylor expansion [30], which results in

$$y'_x = y_x^d + y_x^d \sum_{i=0}^{\infty} k_i r_d^{i-1}, \quad y'_y = y_y^d + y_y^d \sum_{i=0}^{\infty} k_i r_d^{i-1}$$

where $r_d = \sqrt{(y_x^d)^2 + (y_y^d)^2}$.

In this study, we only take into account the parameters k_3 and k_5 that, as stated in [30], are enough to obtain good practical results. These constants are obtained by solving an optimization problem, as proposed in [31]. This method is based on the principle that straight lines in 3-D space should ideally remain straight lines in the 2-D image. A cost function is then defined as the distance between a set of lines in the image and a set of ideal straight lines, and it is minimized with respect to the constants of the inverse radial-distortion function [30]. This method is independent of the calibration process, which is responsible for the computation of the camera intrinsic parameters. Fig. 5(a) and (b) shows the results obtained with the distortion correction method.

VI. EXPERIMENTAL SETUP

To assess the performance of the proposed solution, an experimental setup comprising a MemSense nIMU and an AXIS 215 PTZ camera was mounted on a Model 2103HT motion rate table, which enabled the acquisition of high-accuracy ground-truth data. Fig. 6 shows the experimental setup together with



Fig. 6. Experimental setup.



Fig. 7. Hardware used in the real-time prototype. (a) MemSense nIMU. (b) AXIS 215 PTZ camera.

the set of four colored circles that were used as visual features in the experiments. The circles are placed in the vertices of a rectangle with 0.5 m height and 0.75 m width, and during the experiments, the distance between the feature plane and camera ranged between 1.40 m and 1.60 m.

The Model 2103HT from Ideal Aerosmith [22] is a three-axis motion rate table that provides precise angular position and rate (position accuracy $\pm 0.0083^\circ$ and rate accuracy $0.01\% \pm 0.0005^\circ/\text{s}$).

The MemSense nIMU, shown in Fig. 7(a), is an inertial unit that contains a triad of rate gyros, a triad of accelerometers, and a triad of magnetometers. The data are received via an RS422 communication link with sampling frequency of 150 Hz. The rate gyros have a dynamic range of $\pm 150^\circ/\text{s}$, a typical noise of $0.36^\circ/\text{s}$ (1σ), and a maximum noise of $0.95^\circ/\text{s}$ (1σ).

The AXIS 215 PTZ shown in Fig. 7(b) is a network camera that can be controlled in pan and tilt using stepper motors ($\pm 170^\circ$ pan range, $180^\circ/\text{s}$ pan speed, 180° tilt range, and $140^\circ/\text{s}$ tilt speed). The angular positions and speeds can be set with a resolution of 1° and $1^\circ/\text{s}$, respectively. The interface with the camera is carried out via a local network and using the hypertext transfer protocol (HTTP). The acquired JPEG images have 352×288 pixels, which reflect the compromise reached between image resolution, acquisition time, and processing time. The sampling frequency of the image measurements, which accounts for acquisition and feature extraction, is 10 Hz.

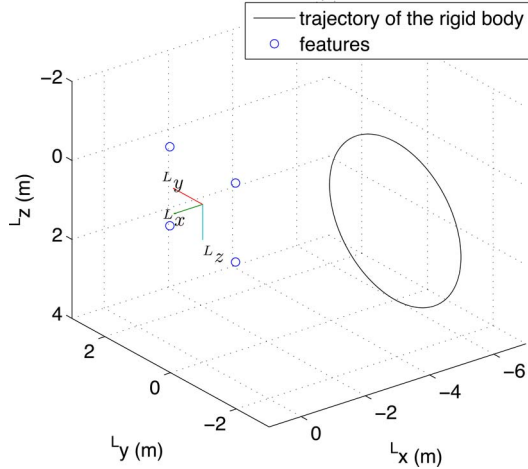


Fig. 8. Rigid body simulated trajectory and position of the features.

VII. SIMULATION RESULTS

To demonstrate the effectiveness of the proposed ensemble, this section illustrates, in simulation, the dynamic behavior of the active camera pan-and-tilt controller and the discrete-time implementation of the attitude observer during a typical vehicle maneuver. The tuning capabilities of the observer and the controller are also displayed for two sets of feedback gains. To test the performance of the observer, we evaluate the convergence of the closed-loop system when the constant bias assumption is not satisfied. We also present a comparison between a single-rate implementation at the lower sampling rate of the camera and the proposed multirate implementation, which explores the high sampling frequency of the rate gyros.

The positions of the features are ${}^L\mathbf{x}_1 = [0 \ -1 \ -1]^T$ m, ${}^L\mathbf{x}_2 = [0 \ 1 \ -1]^T$ m, ${}^L\mathbf{x}_3 = [0 \ -1 \ 1]^T$ m, and ${}^L\mathbf{x}_4 = [0 \ 1 \ 1]^T$ m, which satisfy $\sum_{i=1}^4 {}^L\mathbf{x}_i = 0$ and Assumption 1. The maneuver consists in a circular trajectory with a radius of 2 m, parallel to the ${}^Lx, {}^Ly$, plane, and at a distance of 6 m. The body velocity is aligned with the ${}^B y$ -axis, and during 10 s, it takes the constant value of $-4\pi/12.5$ m/s (≈ 1 m/s). From then onward, it decreases linearly until the starting point of the maneuver is reached with zero velocity. The position of the features and the trajectory of the rigid body is depicted in Fig. 8. To match the conditions of the experimental setup, the sampling rate of the vision system and inertial measurements were set to 10 Hz and 150 Hz, respectively.

The initial estimation errors in the simulations are $\|\tilde{\mathcal{R}}(0) - \mathbf{I}\| = 0.4129$, $\tilde{\mathbf{b}}_\omega(0) = [0.5 \ 0.5 \ 0.5]^T \frac{180^\circ}{\pi}$ /s, and the initial pan-and-tilt camera angles are both set to 10° ; thus, (18) is satisfied by the initial conditions.

Fig. 9 illustrates the stability and convergence of the estimation errors. The time evolution of the norm of the features' centroid, $\|\tilde{\mathbf{y}}\|$, and the actuation imposed by the camera pan-and-tilt controller are shown in Fig. 10. The overshoot on $\|\tilde{\mathbf{y}}\|$ is due to the initial bias estimation error. Note that, as expected, when the camera linear velocity is nonzero, the centroid of the features in the image plane differs from the center of the image. The figures also show that the feedback gains can be used to tune the

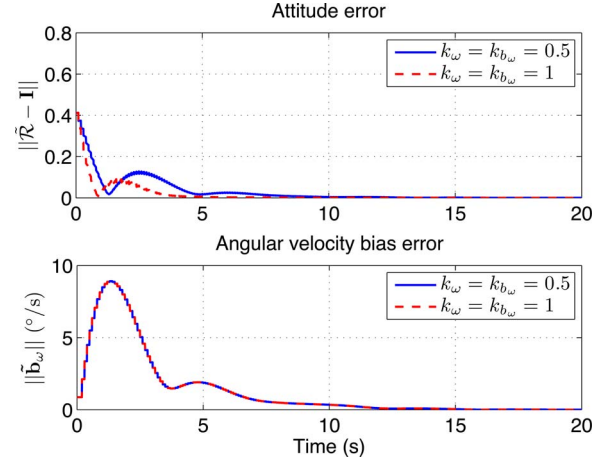


Fig. 9. Attitude observer estimates for two different sets of gains.

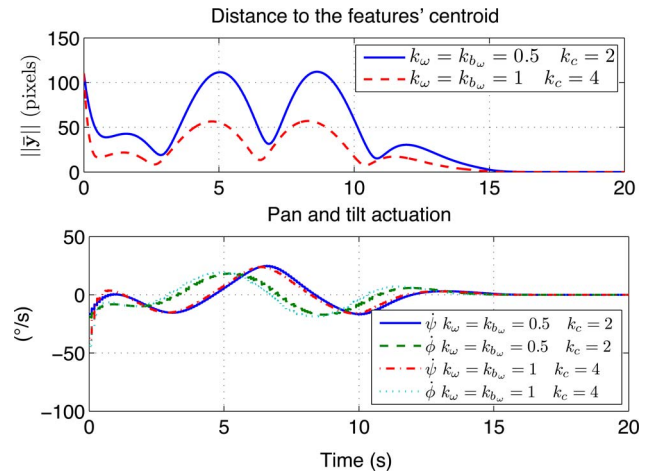


Fig. 10. Distance between the features' centroid and the image center and the pan-and-tilt actuation for two different sets of gains.

convergence characteristics of the observer and the controller. Finally, Fig. 11 depicts the evolution of $\tilde{\mathbf{y}}$ in the image plane.

A. Time-Varying Rate Gyro Bias

The proposed attitude observer was derived under the assumption that the rate gyro bias is constant. If this is not the case, the estimator will not be able to estimate exactly the time-varying offset in the rate gyro measurements. Fig. 12 shows simulation results for two sinusoidal bias signals that vary at different rates. The figure shows that the estimation error no longer converges to zero but remains bounded. Moreover, the simulations also show that the bound increases with the bias derivative, which is the theoretically predicted behavior.

B. Multirate Algorithm

The inertial sensors have much larger bandwidth than visual systems. In our discrete-time algorithm, we exploit this fact to predict the attitude using solely the angular velocity information when the visual information is not available. This is illustrated in Fig. 13, which shows the time evolution of the attitude

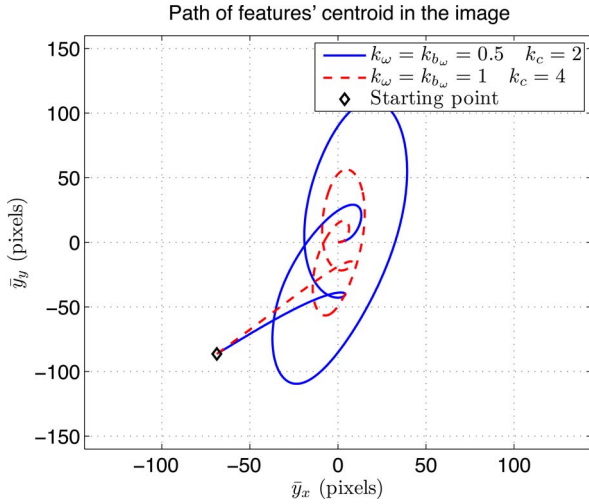


Fig. 11. Path followed by the centroid of the features in the image plane for two different sets of gains.

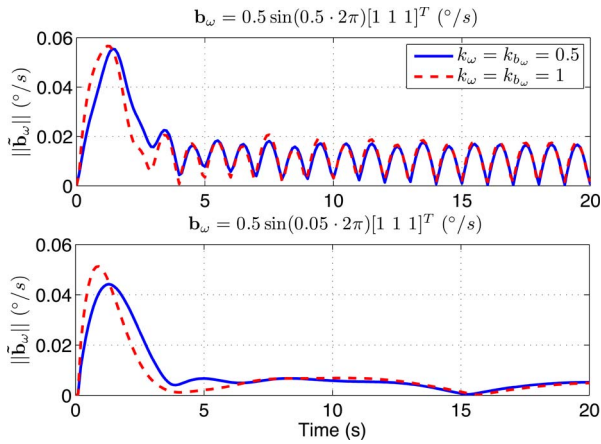


Fig. 12. Simulations with a time-varying rate gyro bias.

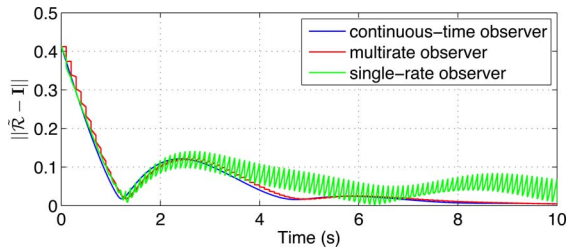


Fig. 13. Attitude estimation error using the continuous-time observer, the multirate observer, and the single-rate observer.

estimation error for the continuous-time, multirate, and single-rate implementations of the observer. Note that the latter does not update the attitude estimate using the angular velocity readings when the visual information is not available.

The figure clearly shows that the multirate implementation provides a much better approximation of the continuous-time observer than the single-rate version and, thereby, leads to smaller estimation errors.

VIII. EXPERIMENTAL RESULTS

This section describes the results obtained in two experiments that attest to the feasibility of the attitude observer and of the

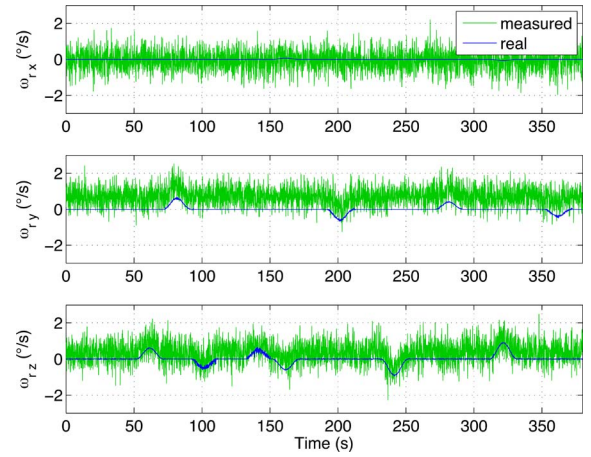


Fig. 14. Angular rate measurements of the first experiment.

ensemble comprising the observer and the camera pan-and-tilt controller. The camera acquires images at 10 Hz, and the rate gyros sampling rate is 150 Hz. In both experiments, the motion rate table described a combination of angular motions in roll, pitch, and yaw, and the distance between the camera and the features ranged between 1.40 and 1.60 m. The camera calibration matrix is given by

$$\mathbf{A} = \begin{bmatrix} \frac{f}{s_x} & -\frac{f \cot \theta}{s_x} & o_x \\ 0 & \frac{f}{s_y \sin \theta} & o_z \\ 0 & 0 & 1 \end{bmatrix}$$

with the focal length $f = 3.8$ mm, the image center $(o_x, o_y) = (320, 240)$ pixels, the effective pixel size in x and y (s_x, s_y) = (0.011, 0.01) mm, and the angle between axes $\theta = 90^\circ$.

A. Using the Measurement Noise to Tune the Observer Gains

Fig. 14 shows the angular rate measurements obtained by the nIMU Memsense during the first experiment, in comparison with the values provided by the calibration table. The measurement noise is characterized by a standard deviation of $0.5443^\circ/\text{s}$, $0.4756^\circ/\text{s}$, and $0.5386^\circ/\text{s}$ (1σ) for the x , y , and z axis, respectively. Regarding the visual features, the measurement noise exhibited a standard deviation of 0.1 pixels.

The technique used to obtain the attitude observer is naturally suited for tackling uncertainties like the presence of a constant bias in the rate gyros but renders the handling of others, like unbiased noise, not straightforward. Nonetheless, we can exploit the information about the measurement noise characteristics in the design of the observer gains. This is accomplished by running the observer in simulation using the experimentally acquired measurement noise and searching for the minimum error over a discrete array of values for the gains k_ω, k_{b_ω} (see Fig. 15). The minimum quadratic error was obtained for the pair $k_\omega = 10^{-0.5}$, $k_{b_\omega} = 10^{-1.75}$.

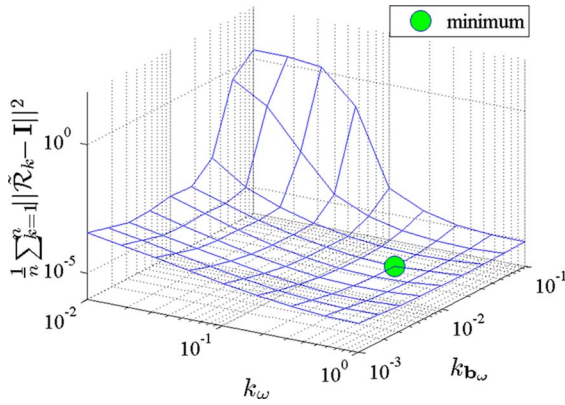


Fig. 15. Average quadratic error for several sets of gains k_{ω} and $k_{b_{\omega}}$.

B. Wahba's Problem

The results were compared with the solution to the classical Wahba's problem [32], which is an optimal algebraic solution to the problem of attitude reconstruction using vector measurements.

Wahba's problem consists in finding the proper orthogonal matrix $\mathbf{R} \in \text{SO}(3)$ such that the loss function

$$J(\mathbf{R}) = \|\mathbf{V} - \mathbf{R}\mathbf{W}\|, \quad \mathbf{V}, \mathbf{W} \in \mathbb{R}^{n \times m}$$

is minimized for a given matrix norm.

Several methods described in the literature handle this problem, namely, the quaternion estimator (QUEST) algorithm, the estimator of the optimal quaternion (ESOQ) algorithm, the Davenport's q -method, whose solution is also based on quaternions, and the singular value decomposition (SVD) algorithm [33].

C. Experiment 1

In the first experiment, the camera controller is idle and the camera stands still. The trajectory is composed by a sequence of angular motions and is such that the visual features remain visible. The initial attitude estimate has an error of 6° in roll, pitch, and yaw.

To illustrate the advantages of the proposed algorithm, we computed, at each instant of time, the solution to Wahba's problem and used it as an alternative attitude estimate for the same experiment. As opposed to the dynamic observer proposed in this paper, the estimation method based on Wahba's problem neglects all knowledge of previous estimates and relies solely on the vector readings extracted from the current image measurements. The resulting attitude estimates are shown in Fig. 16.

Fig. 17 shows the estimation results provided by the method proposed in this paper, which display an increased accuracy and smoothness. Fig. 18 shows the errors of the two methods. The algorithm proposed in this paper produces smaller errors and, in addition, can provide attitude estimates at a much higher sampling rate. The improvement in accuracy is also evidenced by the standard deviation of the estimation errors. The standard deviations obtained with the observer are 0.0641° for roll, 0.3806° for pitch, and 0.3510° for yaw, whereas the standard deviations

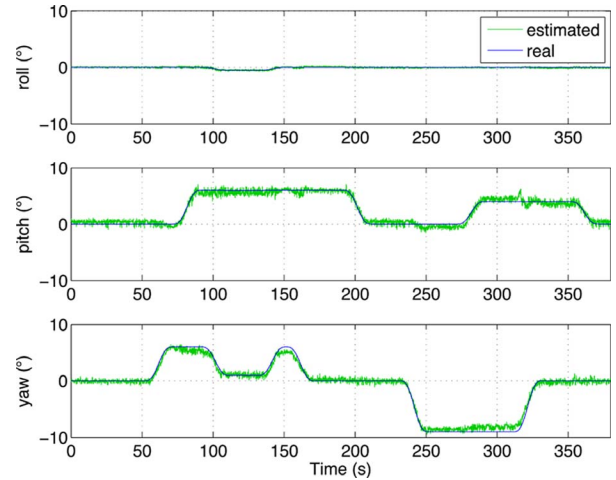


Fig. 16. Attitude determination using the solution to Wahba's problem (Experiment 1).

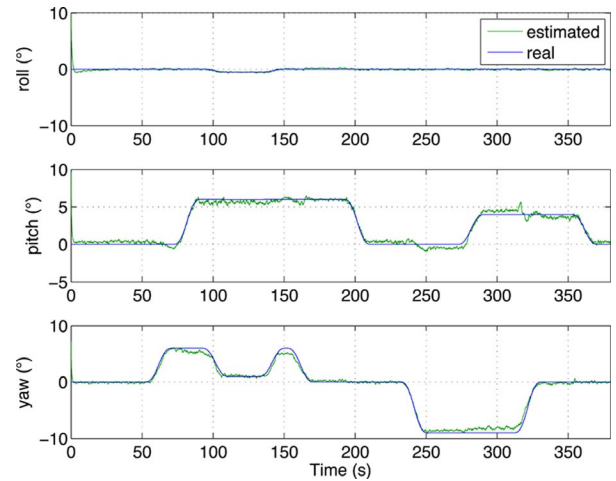


Fig. 17. Attitude estimation using the proposed algorithm (Experiment 1).

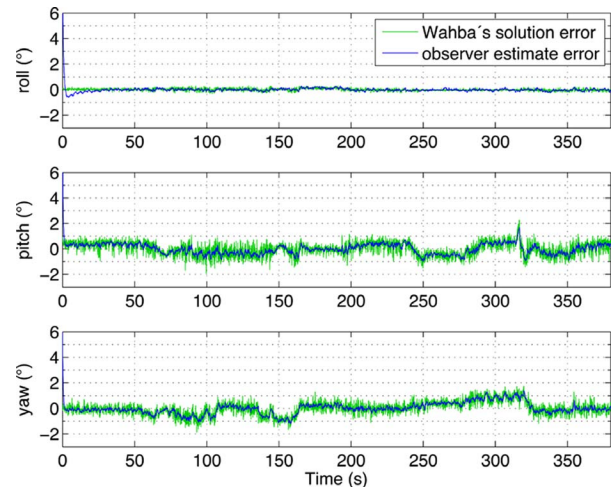


Fig. 18. Comparison between the estimation errors obtained using the Wahba's solution and using the proposed observer (Experiment 1).

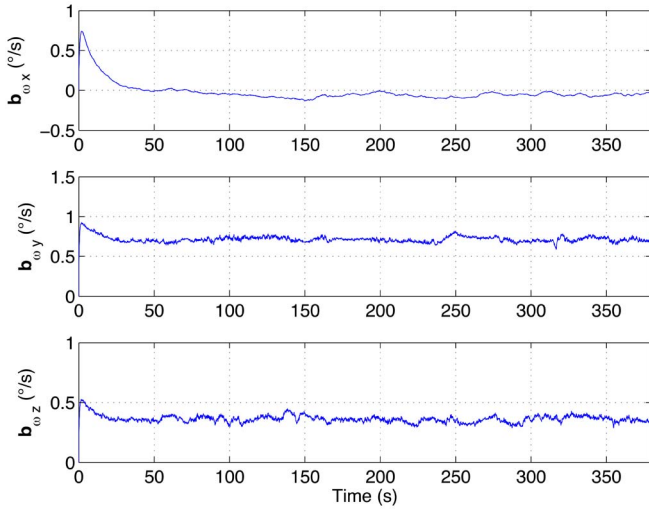


Fig. 19. Angular rate bias estimation (Experiment 1).

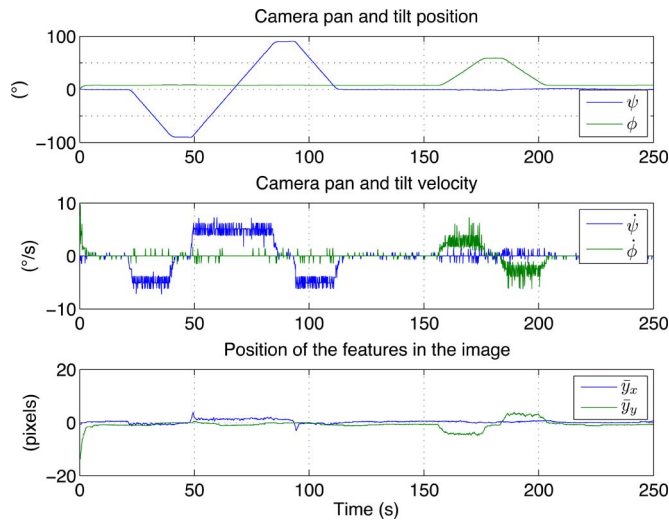


Fig. 20. Time evolution of the camera pan-and-tilt position and velocity and of the features' centroid in the image plane (Experiment 2).

obtained with the Wahba's solution are 0.0924° , 0.5248° , and 0.4635° for roll, pitch, and yaw, respectively.

Fig. 19 shows the time evolution of the angular rate bias estimates. Although, due to the existence of measurement errors, the bias estimates do not reach a constant value, they remain within small intervals.

D. Experiment 2

In the second experiment, the feasibility of the ensemble comprising the attitude observer and the camera pan-and-tilt controller is shown. In contrast with the first experiment, the motion range of the second one requires the control of the camera pan and tilt in order to keep the features visible. This experiment is characterized by a set of motions at constant angular velocity. The observer gains are the same used in the first experiment.

Fig. 20 shows the time evolution of the camera pan-and-tilt position and velocity and the time evolution of the features' cen-

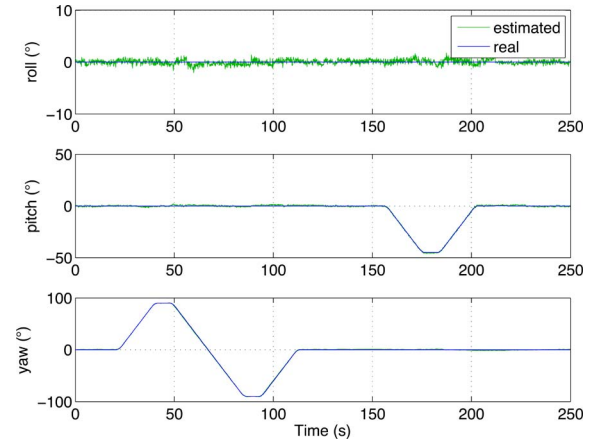


Fig. 21. Attitude determination using the solution to Wahba's problem (Experiment 2).

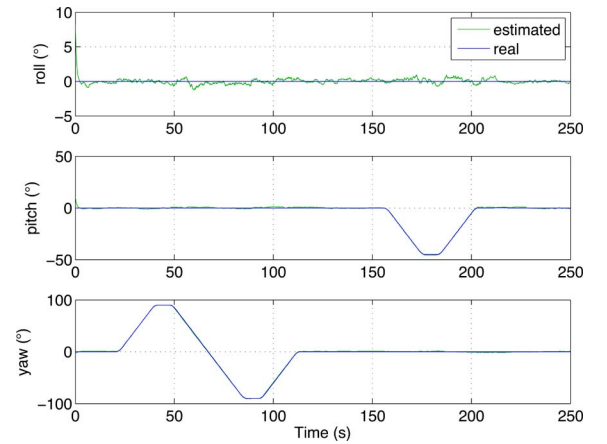


Fig. 22. Attitude estimation using the proposed algorithm (Experiment 2).

triod in the image plane. Despite the reasonable range of movements of the trajectory, the features remain visible throughout the experiment due to the compensation provided by the camera pan-and-tilt controller. Since the yaw angle of $\{B\}$ is in the same rotation axis as the camera pan angle, when this axis rotates, there is no linear velocity and the features' center \bar{y} remains close to center of the image. On the other hand, when there exists a rotation about the pitch angle, the linear velocity is different from zero, and as theoretically expected, \bar{y} is not in the origin.

Figs. 21 and 22 show the attitude estimates obtained using the solution to Wahba's problem and the proposed method.

The errors of the two methods are shown in Fig. 23. As from the previous experience, the errors are smaller using the proposed attitude observer. The standard deviations of the estimation errors obtained with the observer are 0.3318° for roll, 0.4638° for pitch, and 0.8560° for yaw, whereas the standard deviations of the estimation errors obtained with the solution to Wahba's problem are 0.4761° , 0.5739° , and 0.8618° for roll, pitch, and yaw, respectively.

Fig. 24 shows the time evolution of the rate gyro bias estimates. The attitude estimation errors and the variability of the bias estimate are greater in the second experiment than in the

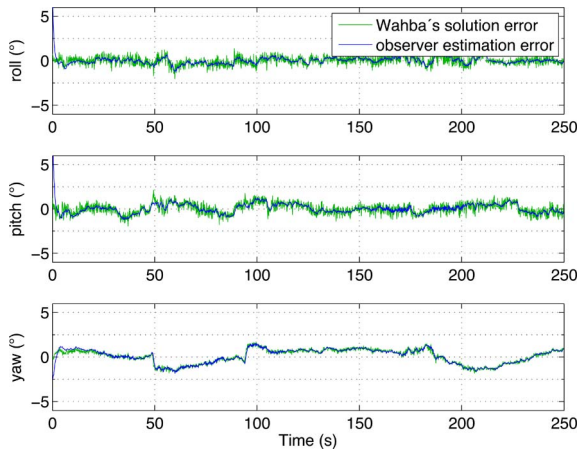


Fig. 23. Comparison between the estimation errors obtained using the Wahba's solution and using the proposed observer (Experiment 2).

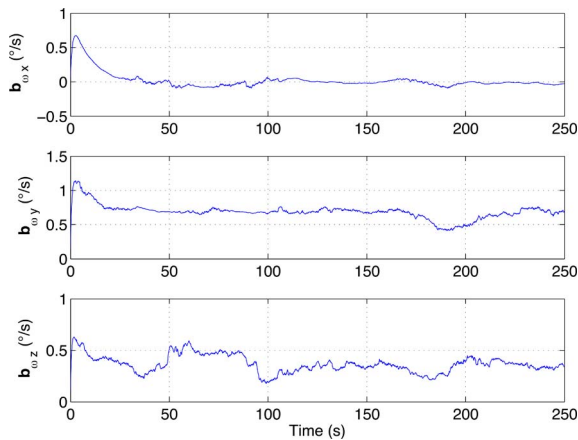


Fig. 24. Angular rate bias estimation (Experiment 2).

first. This is due to the errors introduced by the camera motion and the low accuracy of the pan and tilt angular position and velocity measurements.

IX. CONCLUSION

This paper addressed the problem of estimating the attitude of a rigid body equipped with a triad of rate gyros and a pan-and-tilt camera. An exponential ISS pan-and-tilt control law that enforces feature visibility was introduced. A multirate implementation of the nonlinear attitude observer that takes advantage of the complementary frequency bands of the sensors and uses recent results in geometric numerical integration was proposed. An optimal method for the compensation of the lens distortion was implemented and a gridding technique was used to obtain suitable observer feedback gains. The high level of performance attained by the proposed solution was experimentally demonstrated resorting to a three-axis motion rate table.

ACKNOWLEDGMENT

The authors gratefully acknowledge the contribution of P. Batista during the preparation of the experimental setup.

REFERENCES

- [1] F. Chaumette and S. Hutchinson, "Visual servo control, Part I: Basic approaches," *IEEE Robot. Autom. Mag.*, vol. 13, no. 4, pp. 82–90, Dec. 2006.
- [2] F. Chaumette and S. Hutchinson, "Visual servo control, Part II: Advanced approaches," *IEEE Robot. Autom. Mag.*, vol. 14, no. 1, pp. 109–118, Mar. 2007.
- [3] G. Chesi and A. Vicino, "Visual servoing for large camera displacements," *IEEE Trans. Robot.*, vol. 20, no. 4, pp. 724–735, Aug. 2004.
- [4] YiMa, S. Soatto, J. Kosecka, and S. Sastry, *An Invitation to 3-D Vision From Images to Geometric Model*. (Interdisciplinary Applied Mathematics, vol. 26). New York: Springer-Verlag, 2004.
- [5] H. Rehlinger and B. K. Ghosh, "Pose estimation using line-based dynamic vision and inertial sensors," *IEEE Trans. Automat. Control*, vol. 48, no. 2, pp. 186–199, Feb. 2003.
- [6] J. Lobo and J. Dias, "Vision and inertial sensor cooperation using gravity as a vertical reference," *IEEE Trans. Pattern Anal. Mach. Intell.*, vol. 25, no. 12, pp. 1597–1608, Dec. 2003.
- [7] Y. Yoon, A. Kosaka, and A. C. Kak, "A new Kalman-filter-based framework for fast and accurate visual tracking of rigid objects," *IEEE Trans. Robot.*, vol. 24, no. 5, pp. 1238–1251, Oct. 2008.
- [8] A. I. Mourikis, N. Trawny, S. I. Roumeliotis, A. E. Johnson, A. Ansar, and L. Matthies, "Vision-aided inertial navigation for spacecraft entry, descent, and landing," *IEEE Trans. Robot.*, vol. 25, no. 2, pp. 264–280, Apr. 2009.
- [9] J. F. Vasconcelos, R. Cunha, C. Silvestre, and P. Oliveira, "Landmark based nonlinear observer for rigid body attitude and position estimation," presented at the 17th IFAC World Congr., Seoul, Korea, Jul. 2008.
- [10] R. Mahony, T. Hamel, and J. M. Pflimlin, "Nonlinear complementary filters on the special orthogonal group," *IEEE Trans. Automat. Control*, vol. 53, no. 5, pp. 1203–1218, Jun. 2008.
- [11] J. Thienel and R. M. Sanner, "A coupled nonlinear spacecraft attitude controller and observer with an unknown constant gyro bias and gyro noise," *IEEE Trans. Automat. Control*, vol. 48, no. 11, pp. 2011–2015, Nov. 2003.
- [12] N. Chaturvedi and N. McClamroch, "Almost global attitude stabilization of an orbiting satellite including gravity gradient and control saturation effects," presented at the Amer. Control Conf., Minneapolis, MN, Jun. 2006.
- [13] D. Fragopoulos and M. Innocenti, "Stability considerations in quaternion attitude control using discontinuous Lyapunov functions," *IEEE Proc. Control Theory Appl.*, vol. 151, no. 3, pp. 253–258, May 2004.
- [14] M. Malisoff, M. Krichman, and E. Sontag, "Global stabilization for systems evolving on manifolds," *J. Dyn. Control Syst.*, vol. 12, no. 2, pp. 161–184, Apr. 2006.
- [15] P. E. Crouch and R. Grossman, "Numerical integration of ordinary differential equations on manifolds," *J. Nonlinear Sci.*, vol. 3, pp. 1–33, 1993.
- [16] B. Owren and A. Marthinsen, "Runge–Kutta methods adapted to manifolds and based on rigid frames," *BIT Numer. Math.*, vol. 39, no. 1, pp. 116–142, 1999.
- [17] H. Z. Munthe-Kaas, "Runge–Kutta methods on Lie groups," *BIT Numer. Math.*, vol. 38, no. 1, pp. 92–111, 1998.
- [18] E. Celledoni, A. Marthinsen, and B. Owren, "Commutator-free Lie group methods," *Future Generat. Comput. Syst.*, vol. 19, no. 3, pp. 341–352, Apr. 2003.
- [19] B. Owren, "Order conditions for commutator-free Lie group methods," *J. Phys. A: Math. General*, vol. 39, pp. 5585–5599, 2006.
- [20] J. Park and W.-K. Chung, "Geometric integration on Euclidean group with application to articulated multibody systems," *IEEE Trans. Robot.*, vol. 21, no. 5, pp. 850–863, Oct. 2005.
- [21] C. Budd and M. Piggott, *Geometric Integration and its Application*. (Handbook of Numerical Analysis, vol. 11). Amsterdam, The Netherlands: Elsevier, 2003.
- [22] I. Ideal Aeromsmith. (2006). 2103ht multi-axis table data sheet, rev c [Online]. Available: <http://www.ideal-aeromsmith.com/>
- [23] S. Brás, R. Cunha, J. F. Vasconcelos, C. Silvestre, and P. Oliveira, "Non-linear attitude estimation using active vision and inertial measurements," in *Proc. 48th IEEE Conf. Decis. Control*, Shanghai, China, 2009, pp. 6496–6501.
- [24] S. Brás, R. Cunha, J. F. Vasconcelos, C. Silvestre, and P. Oliveira, "Experimental evaluation of a nonlinear attitude observer based on image and inertial measurements," presented at the Amer. Control Conf., Baltimore, MD, 2010.

- [25] S. P. Bhat and D. S. Bernstein, "A topological obstruction to continuous global stabilization of rotational motion and the unwinding phenomenon," *Syst. Control Lett.*, vol. 39, no. 1, pp. 63–70, Jan. 2000.
- [26] A. Loría, E. Panteley, "Uniform exponential stability of linear time-varying systems: Revisited," *Syst. Control Lett.*, vol. 47, no. 1, pp. 13–24, Sep. 2002.
- [27] H. K. Khalil, *Nonlinear Systems*, 3rd ed. Englewood Cliffs, NJ: Prentice-Hall, 2002.
- [28] E. Hairer, C. Lubich, and G. Wanner, *Geometric Numerical Integration, Structure-Preserving Algorithms for Ordinary Differential Equation*. (Springer Series in Computational Mathematics, vol. 31), 2nd ed. New York: Springer-Verlag, 2006.
- [29] R. Burden and J. Faires, *Numerical Analysis*. Boston, MA: PWS-Kent, 1993.
- [30] T. Thormählen, H. Broszio and I. Wassermann, "Robust line-based calibration of lens distortion from a single view," in *Proc. Mirage*, 2003, pp. 105–112.
- [31] T. Gaspar and P. Oliveira, "A single pan and tilt camera architecture for indoor positioning and tracking," presented at the VISIGRAPP Conf., Lisboa, Portugal, 2009.
- [32] G. Wahba, "Problem 65-1: A least squares estimate of spacecraft attitude," *SIAM Rev.*, vol. 7, no. 3, p. 409, Jul. 1965.
- [33] F. L. Markley and M. Mortari, "Quaternion attitude estimation using vector measurements," *J. Astronaut. Sci.*, vol. 48, no. 2, pp. 359–380, Apr.–Sep. 2000.



Sérgio Brás (S'09) received the B.Sc. and M.Sc. degrees in electrical and computer engineering in 2006 and 2008, respectively, from the Instituto Superior Técnico, Lisbon, Portugal, where he is currently working toward the Ph.D. degree.

His current research interests include nonlinear systems, attitude observers, and inertial navigation systems.

Mr. Brás was the recipient of the Diploma de Mérito during his graduation and the Best Students Award from Universidade Técnica de Lisboa.



Rita Cunha received the Licenciatura degree in information systems and computer engineering and the Ph.D. degree in electrical and computer engineering from the Instituto Superior Técnico (IST), Technical University of Lisbon, Lisbon, Portugal, in 1998 and 2007, respectively.

She is currently a Postdoctoral Researcher with the Institute for Systems and Robotics, IST. Her current research interests include guidance, navigation, and control of autonomous vehicles, nonlinear control, vision-based control, integration of vision and

inertial sensors for attitude and position estimation, and modeling of small-scale helicopters and quadrotors.



José F. Vasconcelos received the Licenciatura and Ph.D. degrees in electrical engineering from the Instituto Superior Técnico, Lisbon, Portugal, in 2003 and 2010, respectively.

Since 2009, he has been a Project Engineer with the Advanced Projects Department, Deimos Engenharia, Lisbon. His current research interests include nonlinear observers, inertial navigation systems, sensor calibration, and robust control with application to autonomous vehicles.



Carlos Silvestre (M'07) received the Licenciatura and M.Sc. degrees in electrical engineering and the Ph.D. degree in control science, all from the Instituto Superior Técnico (IST), Lisbon, Portugal, in 1987, 1991, and 2000, respectively.

Since 2000, he has been with the Department of Electrical Engineering, IST, where he is currently an Associate Professor of control and robotics. Over the past several years, he has conducted research on the subjects of navigation guidance and the control of air and underwater robots. His current research

interests include linear and nonlinear control theory, coordinated control of multiple vehicles, gain-scheduled control, integrated design of guidance and control systems, inertial navigation systems, and mission control and real-time architectures for complex autonomous systems with applications to unmanned air and underwater vehicles.



Paulo Oliveira (S'91–M'95) received the Licenciatura, M.Sc., and Ph.D. degrees in electrical and computer engineering from the Instituto Superior Técnico (IST), Lisbon, Portugal, in 1987, 1991, and 2002, respectively.

He is currently an Associate Professor with the Department of Mechanical Engineering, IST, and a Senior Researcher with the Institute for Systems and Robotics, Associated Laboratory, Lisbon. His current research interests include the area of autonomous robotic vehicles with focus on the fields of estimation, sensor fusion, navigation, positioning, and industrial automation. He is an

author or coauthor of more than 20 journal papers and 100 conference communications. He has participated in more than 20 European and Portuguese research projects over the past 25 years.